

Far-infrared photometry of deeply embedded outflow sources^{*}

D. Froebrich,^{1,4} M.D. Smith,² K.-W. Hodapp³, and J. Eislöffel¹

¹Thüringer Landessternwarte Tautenburg, Sternwarte 5, D-07778 Tautenburg, Germany

²Armagh Observatory, College Hill, Armagh BT61 9DG, Northern Ireland

³University of Hawaii, Institute for Astronomy, 640 N. Aohoku Place, Hilo, HI 96720, USA

⁴Dublin Institute for Advanced Studies, 5 Merrion Square, Dublin 2, Ireland

Released 2003 XXXXX XX

ABSTRACT

We present far-infrared maps and spectroscopy for a number of deeply embedded protostellar objects (Cep E, HH 211-MM, IC 1396 W, L 1157, L 1211, and RNO 15 FIR) from data that we acquired with the ISO instruments PHOT and LWS. Several previously undetected deeply embedded sources are found in the vicinity of our targets. We determine temperatures and luminosities of seven objects and locate them on a L_{bol} - T_{bol} diagram – the equivalent to a Hertzsprung-Russell diagram for protostars. Their masses and ages, according to their location on tracks taken from our evolutionary model, are derived. L 1211 and Cep E appear to be intermediate mass objects which will reach final masses of about $3 M_{\odot}$, while the other sources are in or below the solar mass range. The derived ages of 15000 to 30000 yr are consistent with their current Class 0 state. A comparison of the luminosity of the associated outflows in the 1–0 S(1) line of molecular hydrogen with the source properties (bolometric luminosity, bolometric temperature, and envelope mass) of 16 Class 0 sources shows no statistically significant correlations. Nevertheless, the data are consistent with a scheme in which the outflow strength and protostar evolve simultaneously. We show that the relationship is partially disguised, however, by the local properties of the surrounding material, the extinction, and short-term flux variability.

Key words: Stars: evolution – Stars: formation – Infrared: stars

1 INTRODUCTION

In the earliest stages of star formation – the so-called Class 0 and Class 1 phases – protostars are still deeply embedded in their parental molecular cloud cores. This material absorbs almost all of the emitted radiation of the star in the optical and the near-infrared. The spectral energy distribution (SED) of Class 0 protostars peaks at about 100–160 μ m, the wavelength of the maximum of a modified blackbody at 30–80 K. Hence, direct observations of protostars have to be carried out in the far-infrared and in the (sub-)mm wavelength range. Sub-mm and millimeter observations of some of the sources investigated here have been obtained e.g. by Lefloch et al. (1996), Ladd & Hodapp (1997), Chini et al. (2001), Gueth et al. (1997), Motte & André (2001), and Gueth & Guilloteau (1999).

The ISO satellite (Kessler et al. (1996)) with its PHOT instrument had the capacity to measure the broad-band continuum in the far-infrared. Such observations, covering the peak region of the SED of protostars, help to yield some of the major properties of these objects such as their temperature, the sub-mm slope of their

SED, the optical depth and the solid angle under which they emit. The latter two cannot be disentangled due to the limited spatial resolution of the ISOPHOT instrument. With higher resolution observations (e.g. SCUBA), however, we can independently determine the solid angle under which an object is seen and that way infer its optical depth. These parameters, together with the distance, enable us to calculate the total (L_{bol}) and sub-mm (L_{smm}) luminosities of each object. We may then decide whether an object really is of Class 0 or not by determining the L_{smm}/L_{bol} ratio (André et al. (2000)). Finally, by placing the inferred values on a temperature – bolometric luminosity diagram – the equivalent to a Hertzsprung-Russell diagram for protostars (Myers et al. (1998)) – we are able for the first time to estimate the (model dependent) ages and masses of these sources directly.

Bipolar outflows invariably accompany Class 0 sources: strong inflow and outflow of material are concurrent. We thus wish to probe how the mass outflow rate is related to the mass accretion rate onto the protostar. The outflowing material interacts with the ambient medium through radiative shocks. Thus, the luminosity of the outflow may be correlated with some of the source properties (e.g. the bolometric source luminosity), which depend on the mass accretion rate. Therefore, we measured the luminosities of the outflows of 16 Class 0 sources in the 1–0 S(1) line of molecular hydrogen. This is usually the strongest and easiest line to observe in

^{*} Based on observations with ISO, an ESA project with instruments funded by ESA Member States (especially the PI countries: France, Germany, the Netherlands and the United Kingdom) and with the participation of ISAS and NASA.

Table 1. Log of our ISOPHOT and LWS observations.

Observation number	Object	α (J2000)	δ (J2000)	AOT	t_{exp} [s]
65903003	RNO 15 FIR	03 27 39	+30 13 00	PHT22	670
65903004	RNO 15 FIR	03 27 39	+30 13 00	PHT22	620
65903101	HH 211	03 43 57	+32 00 49	PHT22	670
65903102	HH 211	03 43 57	+32 00 49	PHT22	620
65201107	HH 211	03 43 57	+32 00 52	LWS01	2268
65902801	HH 211 West	03 43 57	+32 01 04	LWS01	3350
66600502	HH 211 East	03 43 59	+32 00 36	LWS01	2912
46601429	L 1157	20 39 06	+68 02 13	LWS01	3390
28200120	L 1157	20 39 06	+68 02 14	LWS01	1958
52902105	L 1157	20 39 06	+68 02 14	PHT22	668
52902106	L 1157	20 39 06	+68 02 14	PHT22	620
54301407	IC 1396W	21 26 06	+57 56 17	PHT22	668
54301408	IC 1396W	21 26 06	+57 56 17	PHT22	620
56300709	L 1211	22 47 17	+62 01 58	PHT22	670
56300710	L 1211	22 47 17	+62 01 58	PHT22	620
56600912	Cep E South	23 03 13	+61 41 56	LWS01	1888
56402111	Cep E	23 03 13	+61 42 27	PHT22	670
56402112	Cep E	23 03 13	+61 42 27	PHT22	620
56601113	Cep E North	23 03 13	+61 42 59	LWS01	1890

near-infrared spectra of shocked molecular hydrogen, and due to the short cooling time of H_2 it is a good tracer of the present interaction of the outflow with the surrounding material. These H_2 luminosities are then compared with various source properties to investigate possible correlations.

Modelling of Class 0 protostars remains in its infancy. Schemes now exist which yield evolutionary tracks, based on relating gas accretion to the dusty envelope (Myers et al.(1998)) and jet thrust to gas accretion (Bontemps et al. (1996), Saraceno et al. (1996), Smith (1998; 2000), and André et al. (2000)). We combine these schemes here in order to test if the simplest assumptions, such as a spherical envelope and a single accreting object, are feasible.

In this paper, we first present our far-infrared ISO maps and spectroscopy, and then summarize the data analysis and how we derive temperatures and luminosities (Sect. 2). In Sect. 3, we present our results, and comment on individual objects. A discussion of age and mass determination, and the general relationship to the outflows is contained in Sect. 4. A framework within which the data can be interpreted is then put forward (Sect. 5).

2 OBSERVATIONS AND DATA ANALYSIS

We used the ISO satellite to obtain ISOPHOT minimaps of six Class 0 sources and LWS full grating spectra for three of them. All observations are listed in Table 1.

2.1 ISOPHOT data

Minimaps were taken for six objects (Cep E, HH 211-MM, IC 1396 W, L 1157, L 1211, and RNO 15 FIR) with ISOPHOT in its PHT22 mode by single pointing and moving of the telescope by one (C100) or half (C200) of a detector pixel. We used four filters (60, 100, 160, and 200 μm). For 60 and 100 μm , the C100 detector (3×3 array of Ge:Ga) was used to create a 5×3 pixel minimap with a pixel size of $45'' \times 46''$. The maps thus cover a field of view of $230'' \times 135''$. For the two longer wavelengths 7×3 mosaics with a pixel size of $45'' \times 90''$ were obtained using the C200 detector (2×2 array of stressed Ge:Ga), covering thus a field of view of $315'' \times 270''$. For details on the instrument and the used Astronomical Observing Templates (AOT) see the ISO Handbook,

Table 2. Observation log of the NIR observations. The used telescopes, detectors and filters are listed. H_2 indicates the narrow band filter, centred at the $1 - 0 S(1)$ line of H_2 . The narrow band filter at a wavelength of 2.140 μm (continuum) is labeled with 2140. The number of images is separately indicated for each filter. In some cases the investigated objects fill only a part of the whole obtained mosaic (esp. HH 212). The observing time is given per single image.

Observatory Date	Telescope Detector	Object	Filter	Number of images	t_{obs} (s)
La Silla Apr93	ESO/MPI 2.2-m IRAC2	HH 24	H_2, K'	12, 3	20, 2
		Ser - FIRS1	H_2, K'	23, 4	20, 2
		VLA 1623	H_2, K'	24, 4	20, 2
Calar Alto Jan94	2.2 m MAGIC	L 1448	H_2, K'	32, 33	60, 3
Calar Alto Sep94	2.2 m MAGIC	DR 21	H_2, K'	437, 78	25, 25
		L 1157	H_2, K'	140, 13	25, 100
Calar Alto Nov95	3.5 m MAGIC	Cep E	$H_2, 2140$	52, 120	30, 30
		HH 211-MM	$H_2, 2140$	60, 59	30, 30
		L 1157	$H_2, 2140$	44, 71	30, 30
		L 1211	H_2, K'	28, 27	200, 60
Calar Alto Sep97	3.5 m MAGIC	Cep A	$H_2, 2140$	202, 368	20, 20
		HH 211	$H_2, 2140$	32, 27	20, 20
		L 1448	H_2, K'	247, 253	20, 3
Calar Alto Nov98	1.2 m MAGIC	Cep A	H_2, K'	64, 32	60, 15
		Cep E	H_2, K'	34, 14	60, 15
		HH 212	H_2, K'	3112, 1487	60, 15
		L 1448	H_2, K'	400, 149	60, 15
		RNO 15 FIR	H_2, K'	120, 60	60, 15
Calar Alto Dec00	3.5 m OMEGA PRIME	Cep E	H_2	24	30
		HH 211	H_2	41	30
		L 1157	H_2	17	30
		L 1448	H_2	42	30

Volume V: PHT — The Imaging Photo Polarimeter¹ and Lemke et al. (1996). The data were reduced with the ISOPHOT Interactive Analysis (PIA V9.1) software.

Flux measurements in the ISOPHOT maps were carried out in two different ways: 1) Point spread function (PSF) photometry using PSF fractions provided by Laureijs (1999) was done for the C100 maps. We do not provide PSF photometry for the C200 detector since the given PSF fractions by Laureijs (1999) are only for the whole C200 pixel and our maps have a sampling of half a pixel in one direction. 2) "Aperture" photometry was obtained for all filters of both C100 and C200 detectors. Here we attributed each pixel in the maps either to 'object' or to 'background' manually, then summed up both and subtracted 'background' from 'object' to obtain its flux. Since at 60 and 100 μm , i.e. for the C100 data, we were able to do photometry with both methods, we have a means of estimating the consistency of both. All measured fluxes, including the available IRAS fluxes of our objects, and the background level in the maps are provided in Table 3.

2.2 LWS data

For three objects (L 1157, Cep E, and HH 211) we have full grating medium-resolution LWS01 scans, which cover a wavelength range from 43 to 196.9 μm with a resolving power between 150 and 300. See the ISO Handbook, Volume IV: LWS — The Long Wavelength

¹ http://www.iso.vilspa.esa.es/manuals/HANDBOOK/V/pht_hb/

Spectrometer² and Clegg et al. (1996) for instruments and AOT details. We reduced the LWS data using standard pipeline 7. For deglitching and flux calibration and defringing of the spectra we employed the ISO Spectral Analyses Package (ISAP 1.6a).

2.3 Near-infrared H₂ observations

For the measurement of the luminosities of the outflows in the 1–0 S(1) line of molecular hydrogen at 2.122 μm near-infrared images were taken in several observing campaigns and at various telescopes. The complete list of all observations is provided in Table 2. We observed the objects in two filters to distinguish between line and continuum emission. Due to the angular size of the objects, the single images had to be arranged into large mosaics. All observing campaigns were (re)-reduced for consistency using own software based on the IRAF package DIMSUM. The whole procedure includes flatfielding, cosmic ray hit removal and sky subtraction as well as re-centering and mosaicing. For a higher astrometric accuracy we used all available stars in the field for the re-centering. The photometric calibration was achieved by the observation of faint near-infrared standards with an accuracy of 10%. For the flux measurements we subtracted the scaled continuum image from the emission line image to measure only the flux in the 1–0 S(1) line of H₂.

Our images are being prepared for publication or are already published. Since in this paper we will only use the integrated H₂ line luminosities we do not reproduce the images here. The objects are discussed in the following papers: RNO 15 FIR in Davis et al. (1997) and Rengel et al. (2002); HH 211-MM in Eislöffel et al. (2003); VLA 1623, L 1157 in Davis and Eislöffel (1995); L 1211 in Froebrich and Eislöffel (2004); Cep E in Eislöffel et al. (1996), Smith et al. (2003); L 1448 region in Eislöffel (2000) and Froebrich et al. (2002); HH 212, HH 24 in Froebrich et al. (2001) and Eislöffel et al. (2004); Ser-FIRS1 in Eislöffel and Froebrich (2004).

2.4 Fit of the spectral energy distributions

The observed broad-band continuum fluxes of our sources allow us to fit a SED to the measurements and to infer source properties (e.g. T_{bol} and L_{bol}). To fit the SED we used Eq. 1 for the flux density S of our objects.

$$S[\text{Jy}] / \Sigma\Omega = (1 - e^{-\tau}) \cdot B(\lambda, T) \quad (1)$$

$B(\lambda, T)$ is the Planck function, $\Sigma\Omega$ the solid angle of the source and τ the optical depth. τ is set as

$$\tau = \tau_{100} \cdot \left(\frac{\lambda}{100\mu\text{m}} \right)^{-\beta}. \quad (2)$$

λ is in μm , the optical depth at 100 μm (τ_{100}) is a free parameter, and β is the sub-mm slope of the SED. The lowest rms of the fit is obtained when the solid angle of the object is determined by

$$\Sigma\Omega = \sum_f \frac{(S_f / \Sigma\Omega) S_f^m}{(\Delta S_f^m)^2} \Bigg/ \sum_f \frac{(S_f / \Sigma\Omega)^2}{(\Delta S_f^m)^2}. \quad (3)$$

f indicates the various used filters, S_f^m the flux measurements in these filters, and ΔS_f^m the error of the measurements. $S_f / \Sigma\Omega$ is calculated by

$$S_f / \Sigma\Omega = \frac{\int_{\lambda=0}^{\infty} (1 - e^{-\tau}) B(\lambda, T) T_f(\lambda) d\lambda}{\int_{\lambda=0}^{\infty} T_f(\lambda) d\lambda} \quad (4)$$

for each filter f separately using the filter transmission curves $T_f(\lambda)$.

To fit a graybody to the measured SEDs of each object, a grid of graybodys was computed (see Eq. 1) in which we varied the three parameters T , τ_{100} , and β . We varied the temperature between 15 and 80 K, in steps of 0.25 K, the optical depth at 100 μm from 0.09 to 40, in logarithmic intervals of 1.5, and the sub-mm slope from 0.0 to 3.0, in steps of 0.1. These graybodys were convolved with the filter curves of the used filter bands (see Eq. 4). Then the solid angle $\Sigma\Omega$ was determined by computing the deviation of the model points from the measurements and minimising this value (see Eq. 3). Finally the rms of the fit to the measurements was calculated (see Eq. 5; n indicates the number of filters) and the parameters leading to the minimal rms were selected.

$$rms = \sqrt{\frac{1}{n} \sum_f \frac{(S_f(T, \beta, \tau_{100}, \Sigma\Omega) - S_f^m)^2}{(\Delta S_f^m)^2}} \quad (5)$$

We find that τ_{100} has almost no influence on the shape of the graybody curve, but only on the absolute flux level, which on the other hand mainly depends on $\Sigma\Omega$. Thus, the values presented in Table 4 are determined by fixing τ_{100} to unity. This restriction has no influence in the deduced parameters T_{bol} and L_{bol} , but the given source size $\Sigma\Omega$ has no physical meaning. In Sect. 3 we present also graybody fits with τ_{100} as a free parameter, in case that this improves the fit significantly. If sub-mm or millimetre observations yield source sizes, the optical depth at 100 μm can be constrained.

Another way to determine physical meaningful radii for the sources is to follow the assumptions of Myers et al. (1998). They adopt an optically thick envelope, a single power law dependence with the frequency of the emissivity and an envelope density proportional to $r^{-3/2}$. Taking Figure 2 in Myers et al. (1998), we can determine the optical depth using $\log \tau_{100} = -\log T_{bol} + 4.28$. We used the bolometric temperatures from Table 4 to derive τ_{100} , and repeated the fit of the SED with this optical depth. This leads to a new solid angle of the source which is the size of the protostellar envelope where τ_{100} has the correct value, according to the assumptions of Myers et al. (1998). In first approximation the solid angle and the optical depth are connected by $\Sigma\Omega^{-1} \propto (1 - e^{-\tau_{100}})$. Thus, we can determine the radius of the envelope where τ_{100} is unity (presented as R_{100} in Table 4). This radius is different from the envelope sizes obtained of optically thin emission by sub-mm or millimeter measurements (e.g. Motte & André (2001) and Chini et al. (2001)).

The above described method to fit the SED was applied to both, the measurements at our four ISOPHOT wavelengths and all available data from Table 3 (except the IRAS 12 and 25 μm points; see below). The inferred object properties from the latter are listed in Table 4. We did not find significant changes in the fit parameters between the two methods, except for L 1211 and partly for RNO 15 FIR. These differences are discussed in Sect. 3.5 and 3.6, respectively. All obtained results are discussed for each object separately in Sect. 3.

IRAS 12 and 25 μm points are excluded from the fit of the SED since recent works show, that these fluxes are usually far above the fit to the SED (see e.g. Chini et al. (2001), Barsony et al. (1998)). Barsony et al. (1998) argue that this excess mid-IR

² http://www.iso.vilspa.esa.es/manuals/HANDBOOK/IV/lws_hb/

Table 3. Integrated far-infrared fluxes for all detected objects, measured with ISOPHOT, and IRAS, as well as SCUBA and IRAM 30-m points from the literature. Columns C₆₀..C₂₀₀ give the fluxes above the background measured with aperture photometry, columns C₆₀^{psf} and C₁₀₀^{psf} the fluxes obtained by PSF fitting. For comparison we list the IRAS fluxes at 12, 25, 60, and 100 μm in columns I₁₂..I₁₀₀. S₄₅₀ and S₈₅₀ give SCUBA fluxes at 450 and 850 μm from the literature. I₁₃₀₀ is the flux at 1.3 mm. All fluxes are in Jansky. In the B₆₀..B₂₀₀ columns we list the background level in the ISOPHOT maps at 60, 100, 160, and 200 μm in MJy sr^{-1} . The * signs mark the additional detected objects in our maps.

Object	C ₆₀	C ₁₀₀	C ₁₆₀	C ₂₀₀	C ₆₀ ^{psf}	C ₁₀₀ ^{psf}	B ₆₀	B ₁₀₀	B ₁₆₀	B ₂₀₀	S ₄₅₀	S ₈₅₀	I ₁₃₀₀	I ₁₂	I ₂₅	I ₆₀	I ₁₀₀
RNO 15 FIR	25.7	51.5	46.7	48.9	24.8	55.5	19	25	92	120	9.2 ⁽⁵⁾	1.4 ⁽⁵⁾	–	0.25 ⁽¹⁾	3.4	47.1	93.6
RNO 15*	3.3	11.9	7.1	10.8	3.7	10.5	19	25	92	120	–	–	–	0.18 ⁽¹⁾	4.2	48.8	82.2
HH 211-MM	3.0	33.8	56.2	54.8	1.9	20.8	42	138	308	331	16.4 ⁽⁵⁾	3.8 ⁽⁵⁾	0.9 ⁽²⁾	–	–	–	–
HH 211 FIRS2*	2.9	13.7	55.3	48.2	1.0	11.3	42	138	308	331	–	–	–	–	–	–	–
L 1157	6.8	37.8	42.0	38.6	5.9	35.8	11	19	63	72	6.0 ⁽⁶⁾	0.9 ⁽⁶⁾	0.4 ⁽⁶⁾	0.25 ⁽¹⁾	0.25	10.9	53.5
IC 1396 W	5.7	19.9	36.6	26.6	4.6	13.8	25	92	210	230	–	–	–	0.25 ⁽¹⁾	0.6	9.7	38.3
IC 1396 W FIRS2*	0.1	1.2	33.2	9.9	0.2	1.2	25	92	210	230	–	–	–	–	–	–	–
IC 1396 W FIRS3*	0.1	1.2	4.6	17.3	0.2	2.3	25	92	210	230	–	–	–	–	–	–	–
L 1211	12.9	36.5	63.0	75.0	10.5	23.4	42	157	254	280	–	–	0.135 ⁽³⁾	2.7	5.7	19.8	63.6 ⁽¹⁾
L 1211 FIRS2*	3.4	17.0	31.6	46.2	2.2	10.9	42	157	254	280	–	–	0.345 ⁽⁴⁾	–	–	–	–
Cep E	55.2	125.8	102.1	81.4	65.4	123.0	35	99	234	293	43.7 ⁽⁶⁾	4.1 ⁽⁶⁾	1.0 ⁽⁶⁾	0.43	5.8	61.0	112.0

(1) upper limit (2) measured at 1.1 mm (McCaughrean et al. (1994)) (3) measured at 1.2 mm (Tafalla et al. (1999)), MMS 4 (4) measured at 1.2 mm (Tafalla et al. (1999)), superposition of MMS 1, MMS 2 and MMS 3 (5) Rengel et al. (2001) (6) Chini et al. (2001)

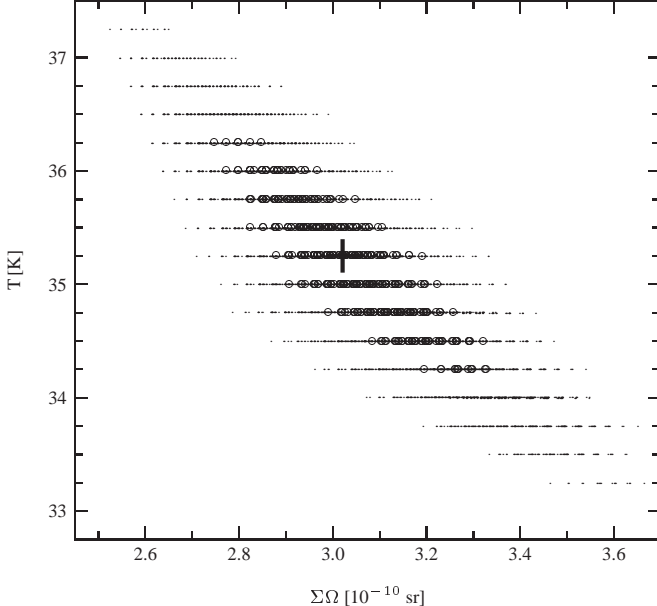


Figure 1. (T, $\Sigma\Omega$) plane for the graybody fit of the Cep E photometry. The fit with the measured fluxes is marked by a cross. Circles indicate fits using fluxes which deviate at most by 0.5 σ , and the small dots represent fits using fluxes with a maximum deviation of 1.0 σ from the measurements.

emission is due to ongoing outflow/dust interactions. Another effect, leading to the detection of these extremely red sources at such short wavelength (and especially at 12 μm) could be the tiniest of red leaks of the IRAS filters. Suppose that there was a red leak of only 0.1 % in the 12 μm filter – at the limit of which the filter transmission curve is known – over the band pass between 20 and 30 μm . The IRAS detectors were still sensitive in this range. Such leak would increase the measured I₁₂ flux of Cep E, for example, by a factor of 500. We also note that the 12 and 25 μm IRAS data points, if used, for most deeply embedded sources show huge deviations from the best-fitting SEDs, compared to the presumed precision of the flux calibration of IRAS. Less red sources, like Class 1 or 2 objects, would hardly suffer from such leaks, because their

SEDs are a lot less steep in the 12 and 25 μm range. Therefore, we decided not to use the IRAS 12 and 25 μm data points in our SED fits for our very red objects.

If one uses the measurements for the determination of the bolometric temperature including also the 12 and 25 μm IRAS points, nevertheless, we get slightly higher values (about 4 K). Since it is not clear how much of this small effect is due to filter leaks, outflow/dust interactions, or envelope emission, we do not list these values in Table 4.

Our best fitting results are given in Table 4 together with the fit errors. In almost all cases it was not possible or not useful to do a fit for the newly detected objects in our maps, since they are at the edge of the map and so we are missing an unknown part of their flux. Some objects are detected only with the C200 detector since they are outside the slightly smaller maps at the C100 wavelengths.

A determination of the fit errors cannot be obtained analytically. Therefore, we varied the measurements within their one sigma error box (five equidistant values; $S_f^m \pm n/2 \cdot \Delta S_f^m$; n = 0, 1, 2) and computed the best fitting parameters for each of the $5^7 = 78125$ combinations. This results in an area of the parameter space into which the error boxes are mapped. As an example, we show in Fig. 1 this area in the (T, $\Sigma\Omega$) plane for Cep E. The errors given in Table 4 are read off such diagrams for each of our objects. This procedure was applied also to the parameters L_{bol}, L_{smm} and T_{bol}.

The determined graybody fits are integrated to obtain the total luminosities of the sources. By integrating only at wavelengths larger than 350 μm we obtain the sub-mm luminosities L_{smm}, which can be compared to the total luminosities L_{bol} to decide whether an object is a Class 0 source (André et al. (2000)). Both values, L_{bol} and L_{smm}/L_{bol}, are given in Table 4. When the ratio L_{smm}/L_{bol} exceeds 0.005, then the object is counted as Class 0. This is equivalent to the mass ratio M_{env}/M_{*} being larger than unity (see André et al. (2000) and references therein). The given bolometric temperatures T_{bol} are the temperatures of a blackbody with the same mean frequency as the graybody, where the mean frequency $\bar{\nu}$ of an SED is determined by

$$\bar{\nu} = \int_0^{\infty} \nu \cdot \text{SED}(\nu) d\nu \Big/ \int_0^{\infty} \text{SED}(\nu) d\nu \quad (6)$$

3 RESULTS

Our observations of Cep E, HH 211-MM, IC 1396 W, L 1157, L 1211, and RNO 15 FIR were carried out at their nominal IRAS positions. In our ISOPHOT maps (shown in Figs. 2–8) we detected more objects than were actually targeted. In four cases other (partly) unexpected embedded objects or bright diffuse continuum emission are found. For L 1211 no object was detected at the nominal IRAS position, but there were two other sources discovered in the maps. Measured fluxes in all filters, including IRAS fluxes and sub-mm and millimeter points from the literature, are given in Table 3.

Discrepancies of the fluxes between PSF and "aperture" photometry are for various reasons: First, it is a major problem to determine which pixel contributes to which object when doing "aperture" photometry. A second problem is the determination of the background. When using the PSF fitting method, the background is determined automatically (provided that the object is a point source and in the centre of a pixel), while for "aperture" photometry one has to choose background pixels. Concerning the absolute calibration errors for the two detectors of 15 and 10% for the C100 and C200 detector, respectively, and an additional error of 20% due to background uncertainties, we find that both flux determination methods lead to consistent results in almost all cases.

Most of our investigated objects are of Class 0 type according to the $L_{\text{smm}}/L_{\text{bol}}$ criterion. We cannot decide whether the newly discovered objects in our maps are of Class 0, because they are situated at the edges of the ISOPHOT maps. Due to the different sizes of the maps we certainly underestimate their fluxes at 60 and 100 μm , which alters their derived SED in the way that they seem to be proportionally brighter at the longer wavelengths, but to an unknown extent.

The ISOPHOT and the IRAS fluxes at 60 and 100 μm are consistent within the errors only for Cep E. For all other objects the IRAS point source catalogue gives values which are a factor of about 1.8 brighter. Apart from the fact that the errors for the IRAS data are quite large and in some cases only upper limits are given, the main reason for the differences is that the resolution of the IRAS satellite was not sufficient to resolve close-by sources. Only Cep E and L 1157 seem not to have other young objects in their immediate vicinity, and these are the two objects where the IRAS and ISOPHOT fluxes match the best. Cep E is a known double source (Moro-Martín et al. (2001)) which cannot be resolved by IRAS nor ISOPHOT. For these reasons and the still fairly large errors in the flux measurements, no investigation of the time evolution of the fluxes of these young sources over the 14 year time span ($\approx 0.1\%$ of the age of our objects) between IRAS and ISO is possible.

The PSF photometry suggests that all the objects are seen as point sources for the ISOPHOT detectors. When subtracting the fitted PSF, no systematic residuals are visible in the difference images. Thus, the angular size of the sources is at maximum 10'', a quarter of the FWHM of the PSF. This leads to an upper limit for the source solid angles of about 100 \square'' . This fact is supported by the inferred sizes R_{100} on the order of 1×10^{-10} sr (4 \square''), which is less than one percent of the pixel size of the C100 detector.

For the three objects for which we obtained a LWS spectrum, we can compare the PHOT flux with the LWS continuum.

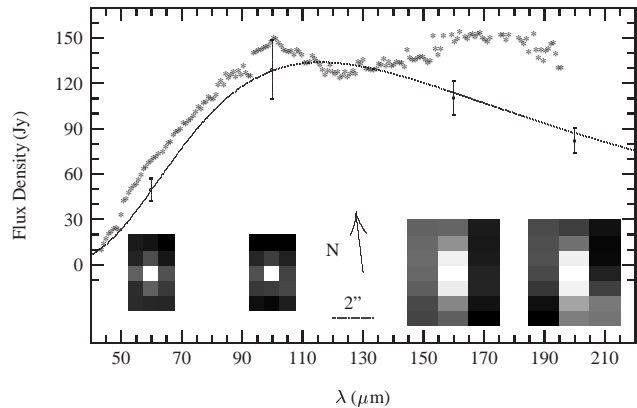


Figure 2. ISOPHOT maps and derived photometry for Cep E. Stars (*) show the LWS spectrum and the solid line the best graybody fit ($T = 35.3\text{ K}$, $\beta = 1.0$, $\Sigma\Omega = 3.0 \times 10^{-10}\text{ sr}$) to the data. τ_{100} is fixed to unity. Error bars for the PHOT data only include the 15% and 10% errors of the detectors. They do not include additional uncertainties due to background determination. The four maps are centred on the central wavelength of the appropriate filter and have the same scale and orientation, given by the scale and the arrow.

While the LWS continuum is a sum of the continuum of the source and background radiation, the PHOT maps give the true flux of the source. So, the difference between LWS and PHOT should be the background radiation (e.g. from cold dust). In all three cases (Cep E, L 1157, and HH 211-MM) we clearly see evidence for such a background emission (see Figs. 2–5).

In the following subsections we discuss details of the results for the individual objects.

3.1 Cep E

Cep E is the brightest object in our sample. Our ISOPHOT maps at the four wavelengths of 60, 100, 160, and 200 μm are shown in the lower part of Fig. 2, all at the same scale and orientation. Photometry from these maps and the LWS spectrum, are displayed above the maps. In addition, we plot the best-fitting graybody to these data as solid line. The fit was used to deconvolve the measurements and the filter transmission curve for converting the measured fluxes to flux densities at the central wavelengths of the used filter. For Cep E, the fluxes determined with PSF and "aperture" photometry were consistent. Deviations of the LWS continuum from the ISOPHOT data exist for wavelengths shorter than 100 and longer than 150 μm . This might be evidence for warm and cold dust.

The PSF photometry shows that the object is a point source, perfectly aligned in the middle of our map, and no other embedded object is detected. Nevertheless Cep E is at least a double source, separated by 1.4'' ($\approx 1000\text{ AU}$), as shown by the 222 GHz observations of Moro-Martín et al. (2001).

Cep E was observed by Chini et al. (2001) with SCUBA (450 and 850 μm) and the IRAM 30-m telescope (1.3 mm). They measured the fluxes in an aperture with a radius of 40'', comparable to the size of our ISOPHOT pixels. The fluxes are given in Table 3. We included these data in the graybody fit. The deduced temperature is 35.3 K for the best graybody fit, which also gives $\beta = 1.0$ and $\Sigma\Omega = 3.0 \times 10^{-10}\text{ sr}$. These parameters are computed fixing τ_{100} to unity. If we vary the optical depth also, the *rms* of the fit is lowered from 0.9 to 0.7. The new graybody parameters are then: $T = 42.8\text{ K}$, $\beta = 1.5$, $\Sigma\Omega = 0.8 \times 10^{-10}\text{ sr}$ and $\tau_{100} = 25$. Nevertheless, the inferred bolometric luminosities and bolometric tempera-

Table 4. Best graybody fit results, as well as the inferred bolometric and sub-mm luminosities, from our ISOPHOT data and (if available) SCUBA and millimeter measurements from the literature. T is the fitted temperature of the graybody, β the sub-mm slope of the SED, and $\Sigma\Omega$ the solid angle of the source. The optical depth at $100\ \mu\text{m}$ was fixed to 1.0, since it did not show significant influence on the shape of the graybody. R_{100} gives the corresponding radius of the envelope where τ_{100} is unity, determined with T_{bol} and following the assumptions of Myers et al. (1998). A discussion of fits with variable τ_{100} can be found in Sect. 3. The rms gives the deviation of the fit from the measurements scaled with the errors of the measurements (see Eq. 5). The explanation of the determination of the errors is given in the text. $\Sigma\Omega$ is given in $1 \times 10^{-10}\ \text{sr}$ (equal to $4.25\ \square''$). The sub-mm luminosity L_{smm} is the luminosity of the object at wavelengths larger than $350\ \mu\text{m}$, and the bolometric temperature T_{bol} is the temperature of a blackbody with the same mean frequency as the object. The * sign marks a newly discovered object. Due to the photometry problems with this object, we do not present errors here.

Object	T [K]	β	$\Sigma\Omega$	R_{100} [AU]	rms	R [pc]	T_{bol} [K]	L_{bol} [L_\odot]	L_{smm}/L_{bol}	Class 0
RNO 15 FIR	34.0 ± 3.0	1.1 ± 0.3	1.7 ± 0.2	270	1.0	350	44.6 ± 3.0	8.4 ± 1.0	0.017 ± 0.007	✓
HH 211-MM	21.0 ± 3.0	1.5 ± 0.6	12.5 ± 1.0	520	2.0	315	31.4 ± 1.0	4.5 ± 0.5	0.046 ± 0.020	✓
L 1157	26.5 ± 1.5	1.4 ± 0.4	3.3 ± 0.3	440	1.5	440	37.8 ± 1.5	7.6 ± 0.8	0.025 ± 0.015	✓
IC 1396 W	30.0 ± 2.0	0.3	1.1 ± 0.2	680	1.3	750	32.6 ± 2.0	16.4 ± 2.0	0.059 ± 0.010	?
L 1211	30.5 ± 2.0	0.0	2.1 ± 0.6	280	1.4	725	30.5 ± 2.0	33.1 ± 4.0	0.073 ± 0.012	?
L 1211 FIRS2*	26.8	0.0	1.7	340	1.6	725	26.9	16.0	0.100	?
Cep E	35.3 ± 3.0	1.0 ± 0.3	3.0 ± 0.4	750	0.9	730	45.0 ± 3.0	77.9 ± 10	0.017 ± 0.010	✓

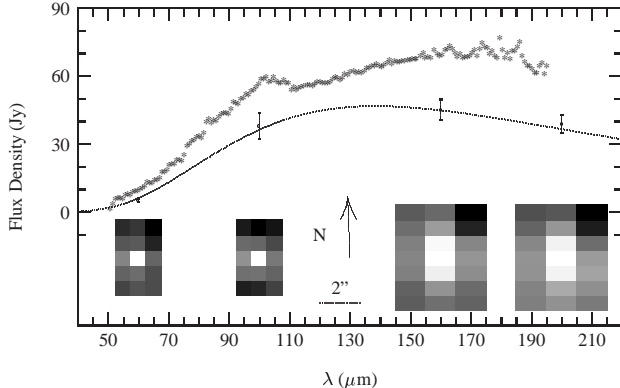


Figure 3. As Fig. 2, but for L 1157. The best graybody has the parameters $T = 26.5\ \text{K}$, $\beta = 1.4$, and $\Sigma\Omega = 3.3 \times 10^{-10}\ \text{sr}$. τ_{100} was fixed to unity.

tures are not affected. We obtain $77.9, 79.6\ L_\odot$ and $45.0, 45.7\ \text{K}$ for a fixed and free τ_{100} , respectively. The L_{smm}/L_{bol} ratio is 0.017, a strong hint for the Class 0 nature of this object, even if we observe the superposition of two sources. Using the assumptions of Myers et al. (1998) and T_{bol} we calculate an optical depth at $100\ \mu\text{m}$ of 9.4. From this we determine a radius of the protostellar envelope where τ_{100} is unity of 750 AU. Thus, the diameter (1500 AU) is in agreement with Moro-Martín et al. (2001) who found that the double system (separation of 1000 AU) is surrounded by a common envelope.

The bolometric temperature of about 45 K is well below the value of 60 K given by Ladd and Hodapp (1997). They used the IRAS data (12, 25, 60, and $100\ \mu\text{m}$) and an $800\ \mu\text{m}$ point to fit the bolometric temperature. Chini et al. (2001) could fit the $100\ \mu\text{m}$ IRAS measurement and the 450, 850 and $1300\ \mu\text{m}$ points. These data still do not cover the emission maximum of the source at about $130\ \mu\text{m}$. For an accurate determination of the temperature, however, the position of the maximum of the SED is needed, which was observed here with ISOPHOT.

3.2 L 1157

Our PHOT maps of L 1157, and the integrated photometry obtained from these maps, are presented in Fig. 3. This figure also shows our LWS spectrum of L 1157, as well as the graybody fit to the

photometry. L 1157 was observed with SCUBA and IRAM 30-m by Chini et al. (2001). They give two different measurements for the fluxes: one for the central source only ($10''$ aperture) and one for the source and the whole envelope (a $55''$ by $30''$ elliptical aperture). The fluxes for the central source are given in Table 3.

L 1157 is a point source with a derived temperature of about $26.5\ \text{K}$, $\beta = 1.4$, and $\Sigma\Omega = 4.3 \times 10^{-10}\ \text{sr}$, under the assumption that τ_{100} is unity. Varying the optical depth does not improve the fit. The bolometric temperature and luminosity are $37.8\ \text{K}$ and $7.6\ L_\odot$, while 2.5% of these account for L_{smm} . This classifies L 1157 as a Class 0 source. According to the scheme of Myers et al. (1998) we determine $\tau_{100} = 13$ and $R_{100} = 440\ \text{AU}$. If we use the fluxes given by Chini et al. (2001) for the envelope, we get a much worse fit and it seems that we have a second cool component in the SED. Thus, the ISOPHOT data reflect the emission of the source itself and not the cold extended envelope.

There are small deviations of the LWS continuum from the PHOT photometry over the whole wavelength range. This could be due to diffuse emission from warm and cold dust, or reflecting uncertainties in the calibration of ISOPHOT or LWS. PSF photometry shows that the object is not at the centre of our map, but rather shifted slightly to the east. This could be a hint for another source nearby or a slight mispointing of the telescope due to the limited accuracy of the IRAS coordinates. Since nothing is known in the literature about a second source, we attributed all the flux to L 1157. PSF fitting to the C200 maps to confirm this was not possible, due to the unknown PSF for our half-pixel sampling in the north-south direction. Also the inferred size of the source ($\Sigma\Omega$) does not support the presence of an additional object.

3.3 HH 211-MM

Our PHOT maps, derived photometry and a LWS spectrum of the HH 211 region are displayed in Fig. 5. HH 211-MM at the centre of our maps is the dominant source at 60 and $100\ \mu\text{m}$. IC 348 IR, probably a heavily embedded B-star (Strom et al. (1974), McCaughrean et al. (1994)), is visible to its north-east (marked by a cross). At longer wavelengths, a very cold source HH 211 FIRS2 further north becomes visible and even dominant. It probably coincides with the object IC 348 MMS (marked by a circle), found by Eislöffel et al. (2003) to be the source of a newly detected outflow north of HH 211. Thus, the fluxes of HH 211 FIRS2 given in Table 3 are

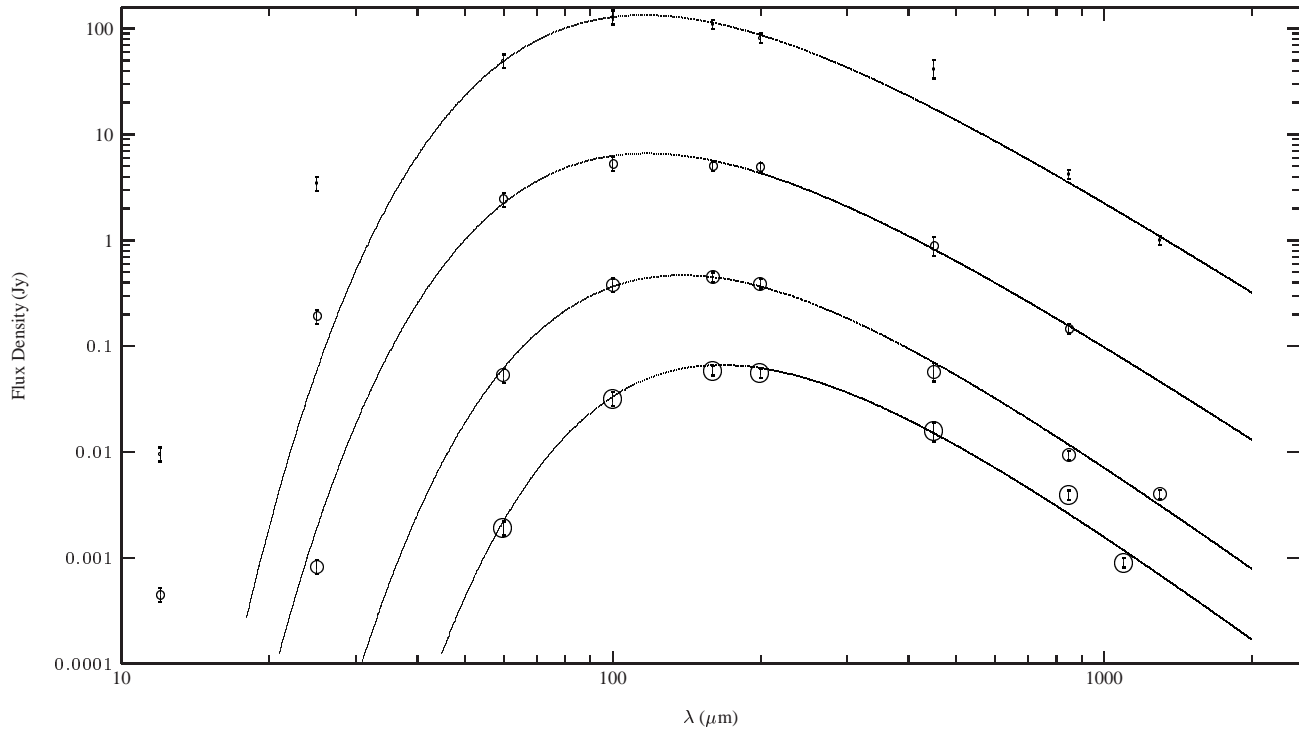


Figure 4. Best obtained fit to the SED using Eq. 1. Overplotted are the IRAS (12 and 25 μm), ISOPHOT (60, 100, 160, and 200 μm), SCUBA (450 and 850 μm), and millimeter (1100, 1300 μm) data points of Cep E, RNO 15 FIR, L 1157, and HH 211-MM (from top to bottom and from small to big circles). τ_{100} was fixed to unity. For the obtained parameters of the best fit see text or Table 4. The models and datapoints are shifted for RNO 15 FIR, L 1157, and HH 211-MM by one, two and three orders of magnitude down, respectively, for convenience. HH 211-MM was not detected by IRAS.

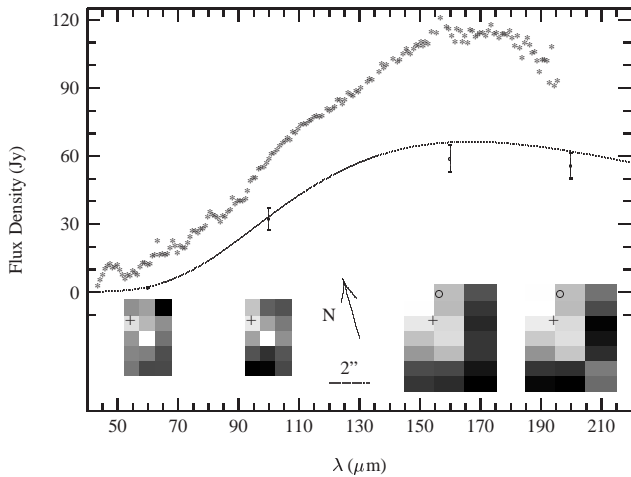


Figure 5. As Fig. 2, but for HH 211-MM. The best graybody has the parameters $T = 21.0 \text{ K}$, $\beta = 1.5$, and $\Sigma\Omega = 12.5 \times 10^{-10} \text{ sr}$. τ_{100} was fixed to unity. The position of IC 348 IR is indicated by a + sign, and a circle marks the source IC 348 MMS, found by Eislöffel et al. (2003).

a superposition of two different objects. The C_{60} and C_{100} measurements are dominated by IC 348 IR, while C_{160} and C_{200} are dominated by IC 348 MMS. Therefore no further investigation of the SED of one of these objects was possible.

For HH 211-MM, we find large differences of the fluxes at 60 and 100 μm obtained with PSF and "aperture" photometry. These differences are due to the other sources influencing the background determination. In addition, there is a lot of diffuse background emission present, which can be seen in Fig. 5 as the difference be-

tween the PHOT photometry and the LWS continuum. So, it is very difficult to determine the background and to state which pixel contributes to the flux of which object. This is further complicated by the fact that HH 211 FIRS2 has a higher surface brightness than our point source HH 211-MM at 160 and 200 μm . Additionally, IC 348 IR could influence our measured flux for HH 211-MM also.

Due to the difficulties in the determination of the fluxes of HH 211-MM we supplemented the ISOPHOT data with SCUBA datapoints at 450 and 850 μm from Rengel et al. (2001) and JCMT bolometry at 1.1 mm from McCaughrean et al. (1994). The fluxes are given in Table 3. We find a fit ($r_{\text{ms}} = 2.0$) with the following object parameters: $T = 21.0 \text{ K}$, $\beta = 1.5$, and $\Sigma\Omega = 12.5 \times 10^{-10} \text{ sr}$. In this case a variable optical depth (instead of a fixed value of unity) does not improve the fit. The inferred bolometric temperature is 31.4 K and the bolometric luminosity is $4.5 L_{\odot}$, while 4.5% account for L_{smm} . This verifies the Class 0 nature of HH 211-MM. According to the low bolometric temperature we find a high τ_{100} on the order of 20 and a large radius for the $\tau_{100} = 1$ surface of 520 AU.

3.4 IC 1396 W

Our PHOT maps and the derived photometry for IC 1396 W are shown in Fig. 6, together with the graybody fit to these data. In the maps, two additional sources are evident. IC 1396 W FIRS2, to the north-east of IC 1396 W, peaks at 160 μm , whereas IC 1396 W FIRS3, to the south-west, is remarkably red, with a flux ratio at C_{200}/C_{160} of 2.6. These additional objects were not detected with the C100 detector, because the maps at these wavelengths are slightly smaller and the objects just fall outside. Nev-

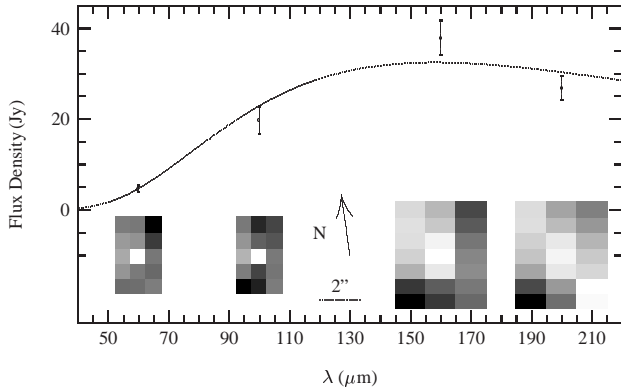


Figure 6. As Fig. 2, but for IC 1396 W. We do not have LWS data for this source. The best graybody fit has a temperature of $T = 30.0$ K, $\beta = 0.3$, and $\Sigma\Omega = 1.1 \times 10^{-10}$ sr. τ_{100} was fixed to unity. Extended cool dust, or a close group of cold sources, are seen northeast of IC 1396 W, while a very cold bright source appears at 200 μ m to the south-west.

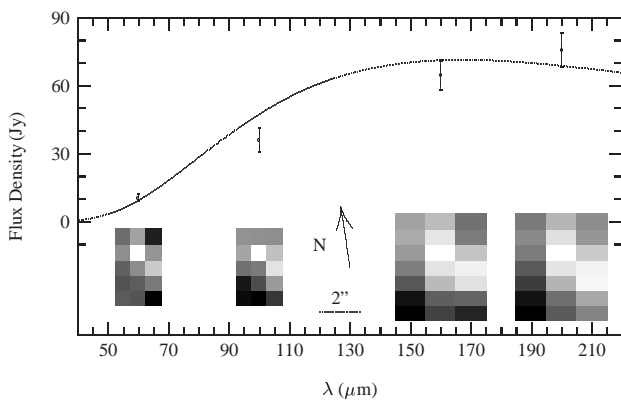


Figure 7. As Fig. 6, but for L 1211. The best fit is a blackbody with $T = 30.5$ K, and $\Sigma\Omega = 2.1 \times 10^{-10}$ sr. τ_{100} was fixed to unity. The object appears north of the nominal IRAS position, and a second cool source is detected south-west of it. See text for the identification of these sources.

ertheless, they influence the flux measurements, especially in the C200 wavelengths range. We do not have observations at longer (sub-millimeter or millimeter) wavelengths to supplement the ISO data.

For IC 1396 W we find a temperature of $T = 30.0$ K, $\beta = 0.3$, and $\Sigma\Omega = 1.1 \times 10^{-10}$ sr for the best graybody fit. These parameters are obtained fixing τ_{100} to unity. A variable optical depth does not improve the fit. The fit is poor ($r_{\text{ms}} = 1.3$), however, suggesting errors in the photometry or a source with dust at more than one temperature. With the graybody parameters we determine a bolometric temperature of 32.6 K, a luminosity of $16.4 L_{\odot}$, and a $L_{\text{smm}}/L_{\text{bol}}$ ratio of 0.059. Concerning the difficulties in the flux measurements and the not available observations at longer wavelengths, the classification of IC 1396 W as a Class 0 source remains questionable. At least sub-mm observations are needed to confirm the presence of a spatially extended envelope, to ensure that we do not just see a compact disk edge-on.

3.5 L 1211

Our PHOT maps of L 1211, the derived photometry, and a graybody fit to these data are displayed in Fig. 7. Somewhat to our sur-

prise, the L 1211 source was not found at its nominal IRAS position, but is shifted a full pixel, corresponding to $45''$ to the north. A second source L 1211 FIRS2, is found in the south-west. Comparing our maps with the work of Tafalla et al. (1999) and Anglada & Rodríguez (2002) we find that our object L 1211 is identical to MMS 4 or VLA 5 and the object L 1211 FIRS2 seems to be a superposition of MMS 3, MMS 2, and MMS 1, and VLA 3 and VLA 1, respectively.

The best fits to both sources are blackbodies ($\beta = 0.0$) and have temperatures of $T = 30.5$ K and $T = 26.8$ K for L 1211 and L 1211 FIRS2, respectively. We infer a solid angle $\Sigma\Omega$ of the sources of 2.1 and 1.7×10^{-10} sr. This results in bolometric temperatures of 30.5 and 26.9 K and in bolometric luminosities of 33.1 and $16.0 L_{\odot}$, for L 1211 and L 1211 FIRS2, respectively. Even if we get quite high $L_{\text{smm}}/L_{\text{bol}}$ ratios (0.073 and 0.100), we cannot firmly establish the classification of the sources as Class 0 objects. This is because our ISOPHOT data do not cover the emission maximum and also L 1211 FIRS2 is a superposition of the emission from several sources.

Tafalla et al. (1999) classify L 1211 as a transitional object between Class 0 and Class 1. They use the IRAS fluxes and an additional observation at 1.2 mm (see Table 3). With these data, as for our ISO data, the maximum of the emission could not be determined exactly. It could only be constrained to lie between 100 and 1200 μ m. With our ISO data, we could corroborate the assumption that L 1211 is of Class 0, since the maximum of the SED is at $\lambda > 160 \mu$ m. If we use the 1.2 mm datapoint from Tafalla et al. (1999) for our analysis, we get a poor fit. Using both, the ISOPHOT and the 1.2 mm point, with plausible values for β (1.0..2.0), the 1.2 mm flux is always overestimated by about one order of magnitude. The same applies for L 1211 FIRS2. Accepting values of $\beta = 3.0$ or higher, we determine $T = 36.3$, $\Sigma\Omega = 3.0 \times 10^{-10}$ sr (L 1211) and $T = 24.8$, $\Sigma\Omega = 5.8 \times 10^{-10}$ sr (L 1211 FIRS2). This leads to bolometric temperatures of about 90 and 46 K and bolometric luminosities of 77 and $19 L_{\odot}$ for L 1211 and L 1211 FIRS2, respectively. The resulting $L_{\text{smm}}/L_{\text{bol}}$ ratios of 0.001 and 0.004 would then classify both objects as Class 1 (L 1211 FIRS2 is still near the transition phase between Class 0 and Class 1).

3.6 RNO 15 FIR

The ISOPHOT maps of the RNO 15 FIR region are shown in Fig. 8, together with the derived photometry and the graybody fit. Visible on our maps are RNO 15 FIR in the centre, and the source RNO 15 to the south-east, marked by a cross. Since this source is warmer than RNO 15 FIR, it is prominent at the shorter wavelengths, but fades considerably relative to RNO 15 FIR towards the longer wavelengths (due to the larger pixel size the two objects also merge). From higher spatial resolution sub-mm maps at 450 and 850 μ m taken with SCUBA (Rengel et al. (2002)) we know that two other objects SMS1 and SMS2 are present to the north and south of RNO 15 FIR, but are merged with it at ISOPHOT resolution (marked by a circle in Fig. 8). They surely influence our flux measurements of RNO 15 FIR.

Since the ISOPHOT measurements show a broad and not well defined maximum of the SED, we supplement these data with SCUBA measurements of Rengel et al. (2001) to determine more accurate source properties. The fluxes at 450 and 850 μ m are measured in a $45''$ by $45''$ aperture (Rengel priv. communication) and listed in Table 3. Using these data in combination with the ISOPHOT points, we get $T = 34.0$ K, $\beta = 1.1$, and $\Sigma\Omega = 1.7 \times 10^{-10}$ sr with an optical depth τ_{100} fixed to unity. The

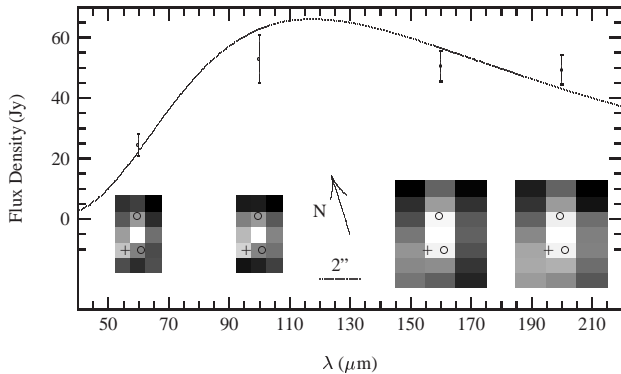


Figure 8. As Fig. 6, but for RNO 15 FIR. The best fit has temperature of $T = 34.0$ K, $\beta = 1.1$, and $\Sigma\Omega = 0.7 \times 10^{-10}$ sr. τ_{100} was fixed to unity. South-east of RNO 15 FIR, the warmer source RNO 15 is detected as well (marked by a cross), especially at the shorter wavelengths. The positions of two other weak sub-mm sources (SMS1 – north, SMS2 – south) are indicated by a circle (Rengel et al. (2001, 2002)).

resulting bolometric temperature and luminosity are 44.6 K and $8.4 L_{\odot}$. 1.7% of the luminosity is in the sub-millimeter regime, classifying RNO 15 FIR as a Class 0 source. If we vary the optical depth at $100 \mu\text{m}$ also, the fit is improved (the *rms* is lowered from 1.0 to 0.6), but the parameters T_{bol} and L_{bol} do not change.

Davis et al. (1997) suggested that RNO 15 FIR might be a double source, due to the observed wiggling in the outflow. This might also be indicated by the deviation of the data points from the determined SED (see Fig. 4).

4 DISCUSSION

4.1 Mass and Age determination

Do Class 0 objects develop into Class 1 and Class 2 protostars? To answer this, we wish to determine basic parameters for the Class 0 protostars, such as age, surrounding mass, present mass and final mass. These, however, are model dependent quantities. In Fig. 9 we plot the locations of our seven (including L 1211 FIRS2) sources on the $L_{\text{bol}} - T_{\text{bol}}$ diagram (large crosses), which is the protostellar equivalent of a Hertzsprung-Russell diagram (Myers et al. (1998)). Also plotted on the diagram are the data for another 37 Class 0 protostars, as listed by André et al. (2000). Two of these sources possess bolometric luminosities above $1000 L_{\odot}$, and so fall outside the display. Note that Class 0 protostars possess bolometric temperatures below ~ 80 K.

The present sample contains quite powerful and cold Class 0 members. Two sources lie above the location of the other explored sources. These are L 1211 and Cep E. As we demonstrate below, such powerful Class 0 sources with low bolometric temperature, can indeed be included in an evolutionary model through the Classes 0–1–2. The large surrounding masses observed restrict the type of model and these objects could go on to produce high-mass stars.

The model tracks plotted represent the evolution of three protostars which end up accumulating masses of 0.2, 1, and $5 M_{\odot}$. The tracks were derived by combining the Unification Scheme, as reviewed by Smith (2000; 2002), with the framework for protostellar envelopes presented by Myers et al. (1998), according to the prescription presented below. We thus determine model ages,

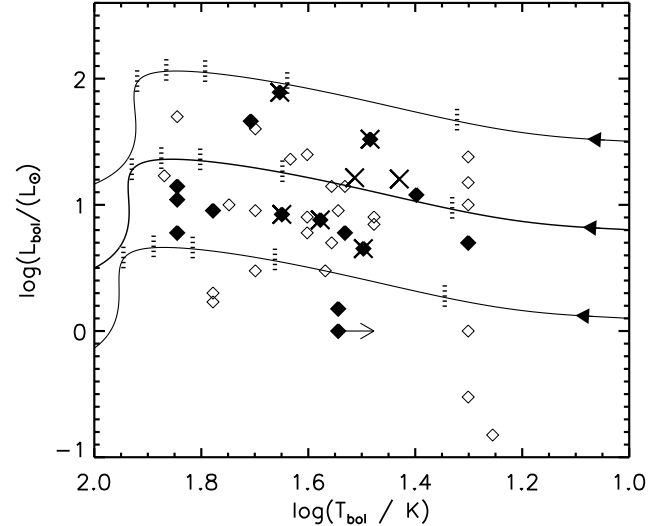


Figure 9. The bolometric luminosity–temperature diagram for the objects analysed here (thick Xs), the Class 0 data from Table 5 (filled diamonds), and the Class 0 data from the review of André et al. (2000) (open diamonds). The superimposed evolutionary tracks are discussed in Section 5. Protostars evolve from right to left. Three tracks for final masses of 0.2, 1, and $5 M_{\odot}$ are displayed. The model peak accretion rate is reached at 17,000 yr, and the power law fall-off is $\propto t^{-7/4}$ with time t , on a 30,000 yr timescale. The vertical dotted lines on the tracks mark the model ages of 20, 30, 40, 50, and 75 thousand years.

present masses of the protostellar nucleus, envelope masses and the final stellar masses (Table 6). The result is that the more massive Class 0 protostars possess large envelopes and would become massive stars. According to the model described here, most of the envelope, however, is not accreted but dispersed, if the majority of protostars here are to form low-mass stars. Note that alternative schemes have been presented by Bontemps et al. (1996), Saraceno et al. (1996), and André et al. (2000). The model envelope masses are in agreement with the measurements. Just for the two objects where we could not determine a proper bolometric temperature (L 1211 and L 1211 FIRS2), there is a significant deviation.

4.2 Outflow Luminosity vs. Source Properties

Is the luminosity of the outflows from the Class 0 sources correlated with the properties of the sources like their bolometric luminosity, the temperature, or mass of their envelopes? To answer this question we measured the luminosity of the outflows from 16 of the Class 0 sources in André et al. (2000) and our objects, in the $1 - 0 S(1)$ line of molecular hydrogen at $2.122 \mu\text{m}$. Due to the short cooling times (some years, Smith and Brand (1990)), H_2 is a good tracer of emission of shocked gas caused by current interactions between outflowing material and the surrounding gas. The $1 - 0 S(1)$ line of H_2 is usually the brightest ro-vibrational line in a spectrum of shocked gas and thus most easily detected.

In magnetohydrodynamic models of Class 0 sources (e.g. Shu et al. (1994), Hirose et al. (1997), and Ouyed and Pudritz (1997)) the accretion rate onto the protostar is connected to the amount of material injected into the outflowing jet. This material interacts with the surrounding quiescent gas in shocks. Hence, the luminosity of these shocks may be connected to the mass accretion rate and thus to the source properties. Here, we tested for correlations of the $1 - 0 S(1)$ H_2 luminosity with the source bolometric lumi-

Table 5. Summary of the Class 0 sources for which a correlation of the source properties with the outflow luminosity in the $1-0\text{S}(1)$ line of H_2 was investigated. Except for our objects observed with ISOPHOT, L_{bol} and T_{bol} are adapted from André et al. (2000), as well as all the M_{env} values (except RNO 15 FIR and L 1211). The outflow luminosities are either from published literature or our own measurements. The typical errors of our outflow luminosities are 10%. In the Ref. column the references are given where we took $L_{\text{H}_2 1-0\text{S}(1)}$ measurements from.

Object	L_{bol} [L_{\odot}]	T_{bol} [K]	M_{env} [M_{\odot}]	$L_{\text{H}_2 1-0\text{S}(1)}$ [$10^{-3} L_{\odot}$]	Ref.
RNO 15 FIR	8.4	44.6	0.9*	0.46	1, 7
HH 211-MM	4.5	31.4	1.5	3.1	2, 7
L 1157	7.6	37.8	0.5	6.1	3, 7
IC 1396 W	16.4	32.6	—	19.0	6
L 1211	33.1	30.5	0.8**	10.7	7
Cep E	77.9	45.0	7.0	70.0	4, 7
L 1448 N	11.0	70.0	2.3	2.16	7
L 1448 IRS2	6.0	70?	0.9	2.8	7
L 1448 C	9.0	60.0	1.4	5.7	7
IRAS 03282	1.5	35.0	0.6	4.46	7
HH 212 MM	14.0	70?	1.2	5.3	5, 7
HH 24 MMS	5.0	20?	4.0	1.21	1, 7
HH 25 MMS	6.0	34.0	0.5	6.61	1
NGC 2264 G VLA2	12.0	25.0	2.0	7.75	3
VLA 1623	1.0	<35	0.7	0.81	3, 7
Ser-FIRS1	46.0	51.0	3.0	0.64	7

* taken from Rengel et al. (2003)

** taken from Tafalla et al. (1999)

References: (1) Davis et al. (1997) (2) McCaughrean et al. (1994) (3) Davis & Eislöffel (1995) (4) Eislöffel et al. (1996) (5) Zinnecker et al. (1998) (6) Froebrich & Scholz (2003) (7) own measurements

nosity, the bolometric temperature and the mass of the surrounding protostellar envelope given by André et al. (2000). The results of these comparisons are shown in Figs. 10, 11, and 12. We obtained a linear regression for each case and tested if the slope of the regression line differed statistically significantly from a slope value of zero. With a probability of error of 5 % none of the regression lines differs from a constant value. Additionally a Kolmogorow-Smirnow-Test shows, that with a probability of error of 0.1 % the data is not consistent with a constant value. Thus, a significant correlation of the outflow luminosity in the $1-0\text{S}(1)$ line of H_2 with any source parameter was not found.

The lack of such correlations may have various explanations. For example, in each outflow, we observe H_2 emission at various distances from the source and these knots or bow shocks are indicating material which was ejected from the source at different times in the past (Δt = distance to the source/jet velocity). Also, the knot luminosity depends on the local properties of the surrounding gas (e.g. gas density, atomic fraction). Additionally, the extinction gradient in the K-band along the outflow is not known. It will alter the measured relative and total fluxes in the sense that knots closer to the source appear fainter due to higher extinction. In Section 5, however, we argue that the location on these diagrams depends sensitively on both mass and age, which results in a wide scatter. Therefore, the lack of a significant correlation of the present source properties and the outflow luminosity in the $\text{H}_2 1-0\text{S}(1)$ line may not be surprising.

A better tool for comparing the outflows to source proper-

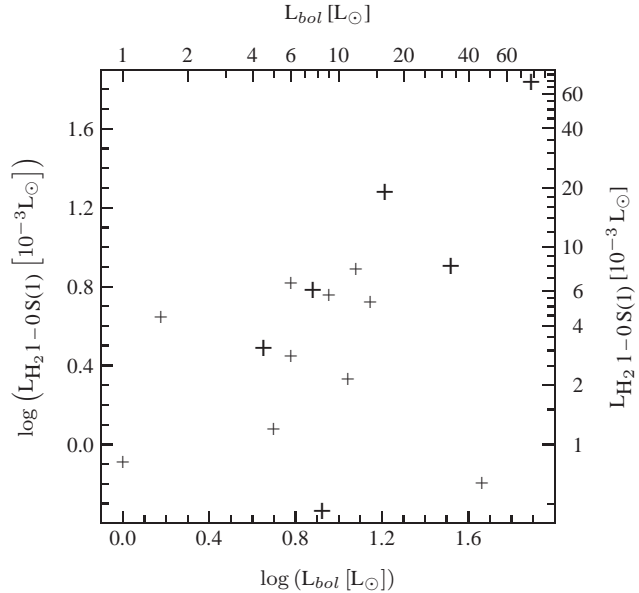


Figure 10. Measured outflow luminosity in the $1-0\text{S}(1)$ line of H_2 versus the bolometric source luminosity for the sources listed in Table 5. The objects investigated in this paper are marked with a large + sign. No significant correlation is found for this sample.

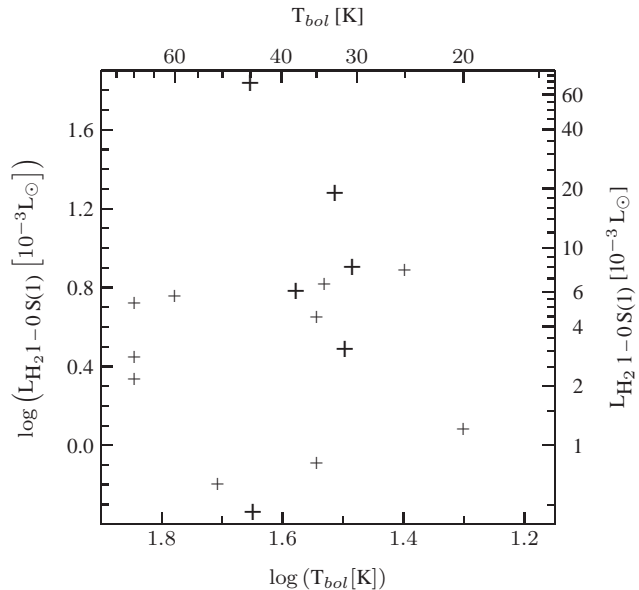


Figure 11. As Fig. 10 but for the bolometric temperatures of the Class 0 sources from Table 5. No significant correlation is found for this sample.

ties may be an optically thin line of CO (e.g. the $1-0\text{^{13}CO}$ line), which should give a measurement of the time-integrated power of the outflow without being influenced by local extinction effects. Comparable observations in the same transition and isotope of CO are needed for a statistically reasonable sample of objects to study their behaviour. At present, only small samples of Class 0 sources have been thus analysed (e.g. Bontemps et al. (1996), Smith (2000; 2002)).

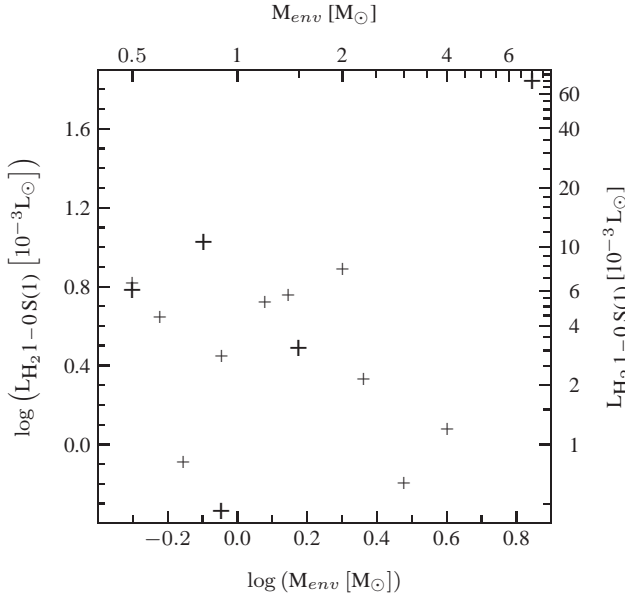


Figure 12. As Fig. 10 but for the envelope masses of the Class 0 sources from Table 5. For IC 1396 W we do not have measurements of the envelope mass. No significant correlation is found for this sample.

5 AN EVOLUTIONARY SCHEME

An evolutionary model for protostars is presented in the Appendix. The outflow scheme has been elaborated by Smith (1998; 2000; 2002) and applied by Davis et al. (1998), Yu et al. (2000), and Stanke et al. (2000). It is based on a prescribed accretion rate from an envelope. Modelling of outflows has demonstrated that the fraction of mass which escapes through jets must reach a maximum during the Class 0 stage. This is required to account for the excess momentum and power of Class 0 bipolar outflows, as calculated from observations of emission lines of CO rotational transitions (see Smith (2000)). We outline in the Appendix the fundamental formulae of the evolutionary scheme.

According to previous modelling of the envelope, three parameters must be introduced to generate plausible models for the bolometric temperature. As shown by Myers et al. (1998), these are (1) the envelope's outer temperature (here $T_o = 24$ K), (2) the efficiency of accretion of the envelope into the star-jet system and (3) the difference in evolutionary timescale between the envelope and the protostar. The envelope consists of material which will fall onto the central object as well as mass directly lost soon after the Class 0 stage. This extra mass component proves necessary to produce a low bolometric temperature, as observed for the Class 0 sources, yet must be rapidly lost in order to yield T Tauri stars within a reasonable time (Myers et al. (1998)).

Previously, we modelled the envelope evolution by assuming mass conservation. Here, we find two significant adjustments are necessary in order to model the new data and maintain plausible time scales. First, the initial mass in the envelope which will eventually fall inwards is reduced to 87% of the total required mass to form the star and excavate the bipolar outflow. The other 13% is presumed to initially lie within a flattened disk. This yields the values in the column 'infall mass' in Table 6.

In Fig. 9, we plot the sample summarised in Table 5 for Class 0 sources for which a correlation of the source properties with the outflow luminosity in the 1-0 S(1) line of H₂ has been investigated. Note that this sample includes warmer and less luminous

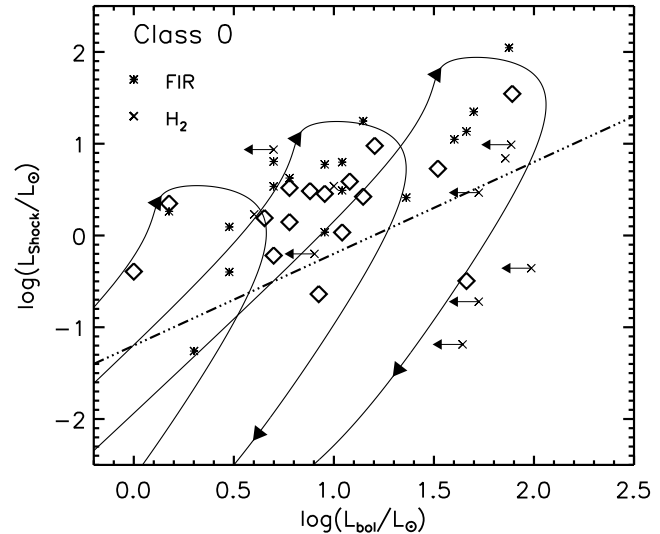


Figure 13. The derived outflow shock luminosity versus the bolometric source luminosity for the Class 0 sources listed in Table 5, as well as the Class 0 sample investigated by Stanke (2000) (symbol: 'x') and the far-infrared line ISO luminosities presented by Giannini et al. (2001) (symbol: '*'). The model tracks are for the same three models presented in Fig 9 and the straight line divides model Class 0 and model Class 1 protostars, as determined by the protostar possessing half of its final mass.

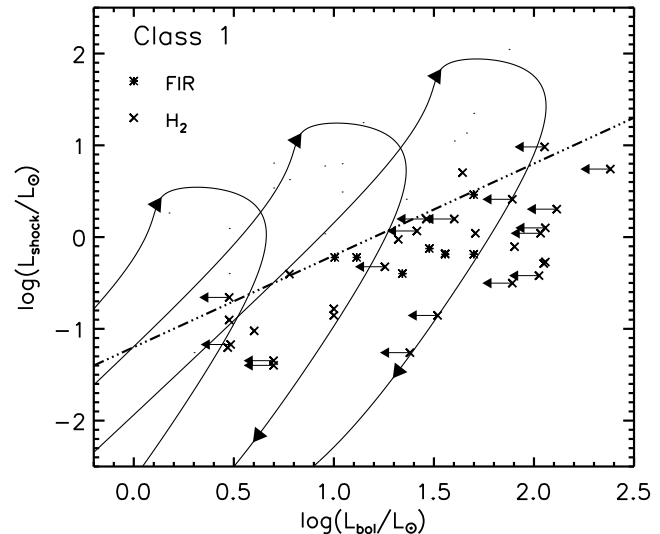


Figure 14. The derived outflow shock luminosity versus the bolometric source luminosity for Class 1 sources from the sample of Stanke (2000) (symbol: 'x') and the far-infrared line ISO luminosities presented by Giannini et al. (2001) (symbol: '*'). The model tracks are for the same three models presented in Fig 9 and the straight line divides model Class 0 and model Class 1 protostars, as determined by the protostar possessing half of its final mass.

protostars than in the ISOPHOT sample investigated above. According to the tracks, this corresponds to a wide range in final stellar masses. The lowest mass star forming here is found to be VLA 1623 (assuming $T_{bol} = 35$ K) which will reach just $0.07 M_{\odot}$, owing to its low bolometric luminosity of only $1 L_{\odot}$ (André et al. (2000)). The low final mass is a result of this version of the evolutionary scheme employed, for which we maintain the same accretion timescale but alter the accretion rate to generate the tracks. This implies that the

Table 6. Parameters derived for the seven objects from the model evolutions. The minimum mass is the total mass with density distributed as $\rho \propto r^{-3/2}$ necessary to provide an optically thick sphere out to a radius R_{bol} , corresponding to the observed T_{bol} . The infall mass is the envelope mass which remains to be accreted (a part of which will escape in the jets), and the envelope mass is the total mass predicted on projecting the distribution out to a radius corresponding to the chosen ambient temperature of 24 K. The model mass accretion rate decreases as $t^{-7/4}$ on a 30,000 yr timescale. The age is given in 10^3 years, the masses are in solar masses. For comparison we give the measured values for the envelope masses from the literature in column M_{env} . The values correspond to the M_{env} column in Table 5. The envelope mass for L 1211 FIRS2 is taken from Tafalla et al. (1999).

Object	Age	Mass	Final	Min.	Infall	Env.	M_{env}
				mass	mass	mass	mass
RNO 15 FIR	29.7	0.10	0.5	0.05	0.32	1.0	0.9
HH 211-MM	24.0	0.06	0.3	0.19	0.26	1.4	1.5
L 1157	27.0	0.10	0.5	0.10	0.35	1.3	0.5
IC 1396 W	24.9	0.21	1.2	0.50	0.88	4.2	—
L 1211	24.0	0.43	2.6	1.53	1.91	10.3	0.8
L 1211 FIRS2	22.5	0.21	1.4	1.42	1.06	6.9	2.1
Cep E	30.6	0.97	4.2	0.37	2.83	8.1	7.0

final mass is nearly proportional to the peak accretion luminosity. Future statistical studies will lead to revisions of this first model.

The simplest form of the unifying model, assumed here, is that a fraction of the jet power is instantaneously dissipated in shock waves, while the bipolar outflow is a time-averaged recording of the momentum outflow. To model the outflow, we have previously employed the H_2 luminosity, $L(H_2)$, which we estimate to be ten times the $1-0S(1)$ luminosity. This is consistent with expectations from shock physics and allows a comparison with previous diagrams presented by Stanke (2000) and Smith (2002). Here, however, we shall use the jet power itself as the comparison parameter. For the comparison, we assume that the observed emission is produced in the warm shocks where the jets dissipate their energy, L_{shock} .

The fraction of the jet power dissipated in molecular hydrogen lines is taken to be 2 %. This is consistent with numerical simulations and bow shock modelling which predict, typically, 10 % of the infrared radiation from shocks in dense clouds to be in the form of H_2 lines. We also assume that 80 % of the jet energy is hidden by just under two magnitudes of K-band extinction. The shock power has also been estimated from the far-infrared lines of CO, OI, OH, and H_2O , measured by ISO (Giannini et al. (2001)). Here, we shall assume that these lines in total, within the ISO-LWS beam, also represent 2 % of the jet power, L_{shock} . We thus increase estimated H_2 and sub-mm luminosities by 50 to yield the displayed values. While these approximations are far from ideal, they permit us to determine if the evolutionary scheme is plausible.

Figure 13 demonstrates that the Class 0 protostars possess almost exclusively high ratios of L_{shock}/L_{bol} . Two objects, however, RNO 15 FIR and Ser-FIRS1, lie well within the model Class 1 regime. Environmental factors could cause a downward shift of the data points, including higher extinction or radiative shocks which are less efficient in H_2 vibrational excitation. Furthermore, these data are consistent with the same model tracks fitted to the bolometric luminosity-temperature data. The lack of a correlation in the data is thus put down to the combination of the distributions in both mass and age.

In addition, previously measured Class 1 outflows almost all

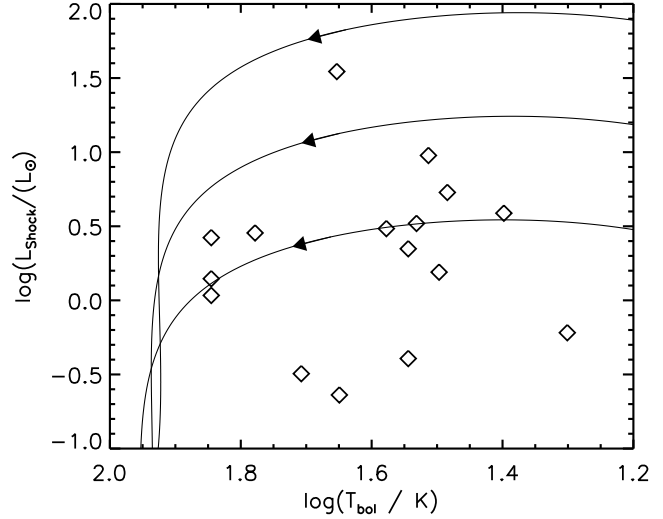


Figure 15. The derived outflow shock luminosity versus the bolometric source temperature for the Class 0 sources listed in Table 5. The model tracks are for the same three models presented in Fig 9.

lie below the predicted Class border line, as shown in Fig. 14. Note, however, that for many of the H_2 flows in Orion detected by Stanke (2000) only upper limits for the bolometric luminosity are available. Nevertheless, the division of the two Classes with the model straight line where the protostar has acquired half the final stellar mass, is evident. A similar difference in outflow luminosity between Class 0 and Class 1 sources has been found by Bontemps et al. (1996).

Figures 15 demonstrates that the model is also consistent with the envelope properties. The main exceptions apparent from this diagram are a group of low luminosity H_2 objects. This suggests that the extinction for these sources may far exceed the fiducial two magnitudes.

6 CONCLUSIONS

We have observed the spectral energy distributions for the six deeply embedded objects Cep E, L 1211, IC 1396 W, L 1157, HH 211-MM, and RNO 15 FIR in the far-infrared with ISO. The inferred temperatures and L_{smm}/L_{bol} ratios confirm the Class 0 nature of four of these sources, within the errors. Employing an evolutionary scheme, we are able to estimate the age, surrounding mass and the current and final mass of these sources. These estimates are, however, model dependent. Two sources, Cep E and L 1211 appear to develop into intermediate mass stars, while the others will become solar mass stars or lower mass objects. The comparison of the ISOPHOT and LWS observations for three of the sources reveals the existence of emission from cold dust in the immediate vicinity of the objects.

A comparison of the luminosity in the $1-0S(1)$ line of H_2 of the related outflows for 16 Class 0 sources, with the source bolometric luminosity, bolometric temperature, and envelope mass was done. We found no statistically significant correlation of the outflow luminosity with each of these source parameters. This could be due to the H_2 luminosity mainly depending on the local properties of the surrounding gas.

The unifying scheme, however, explains the lack of correlations as due to evolutionary effects. Furthermore, the scheme which

involves a redistribution of mass between envelope, disk, protostar, jets and outflow, accounts for the differences in source properties according to the Class.

ACKNOWLEDGEMENT

We thank Manfred Stickel from MPIA for his help with the data reduction of the PHOT data. We thank Alex Rosen for a critical reading of the manuscript and the Department of Culture, Arts and Leisure, Northern Ireland for financial support. Jochen Eislöffel and Dirk Froebrich received financial support from the DLR through Verbundforschung grant 50 OR 9904 9.

The ISOPHOT data presented in this paper were reduced using PIA, which is a joint development by the ESA Astrophysics Division and the ISOPHOT Consortium with the collaboration of the Infrared Processing and Analysis Center (IPAC). Contributing ISOPHOT Consortium institutes are DIAS, RAL, AIP, MPIK and MPIA.

The ISO Spectral Analysis Package (ISAP) is a joint development by the LWS and SWS Instrument Teams and Data Centers. Contributing institutes are CESR, IAS, IPAC, MPE, RAL and SRON.

APPENDIX

We present and test a model based on the transfer of gas between components. We take a spherical envelope of gas and dust, and prescribe an accretion rate from the inner edge of the envelope onto a disk. Note that we assume a centrifugal barrier at 30 AU, which defines the inner envelope – outer disc transition. The accretion disk processes most of the mass onto the protostar and a fraction into twin jets. The speed of the jets is assumed to be a fixed fraction of the escape speed from the protostellar surface.

The accretion rate from the envelope is taken to increase exponentially for a short period before decreasing as a power law through the Class 0, 1 and 2 phases. The zero point of time is thus defined as the moment when accretion starts and, simultaneously, a central hydrostatic object forms. The accretion rate is

$$\dot{M}_a(t) = \dot{M}_o(e/\alpha)^\alpha (t/t_o)^{-\alpha} \exp(-t_o/t). \quad (7)$$

Energy release through accretion and contraction are included. In the models shown, the peak accretion rate is reached at $t_o/\alpha = 17,000$ yr, and the power law index is $\alpha = 7/4$, on a $t_o = 30,000$ yr timescale. The accreted mass is predominantly accrued by the growing protostars. The fraction $\epsilon(t)$ which escapes through twin jets reaches a maximum of $\eta = 0.2$ at the peak accretion time:

$$\epsilon = \eta \left[\frac{\dot{M}_a(t)}{\dot{M}_o} \right]^\zeta \quad (8)$$

where $\zeta = 2$ is found to be appropriate. Hence the mass left over, which accretes onto the core to form the star is

$$M_*(t) = \int_0^t (1 - \epsilon) \dot{M}_a. \quad (9)$$

To form a star like the Sun, this model will provide an early accretion peak in which $\dot{M}_a \sim 10^{-4} M_\odot \text{ yr}^{-1}$ for 10^4 years, and eventually becoming $\dot{M}_a \sim 10^{-7} M_\odot \text{ yr}^{-1}$ for 10^6 years, corresponding to Class 0 and Class 2 or Classical T Tauri stars, respectively. The power-law has substantial observational support (Calvet et al. (2000)).

We previously modelled the envelope evolution by assuming

mass conservation. Here, we make two significant adjustments in order to model the new data. First, the initial mass in the envelope which will eventually fall inwards is reduced to 87% of the total required mass to form the star and excavate the bipolar outflow. The other 13% is presumed to initially lie within a flattened disk. This yields the values in the column 'infall mass' in Table 6. The total mass can be written analytically in terms of an incomplete Gamma function on integrating Eqn. 7:

$$M_{\text{infall}}(t) = \dot{M}_o t_o (e/\alpha)^\alpha [1 - \Gamma(\alpha - 1, t_o/t)]. \quad (10)$$

Secondly, we find that the low bolometric temperatures of Class 0 protostars can only be attained by introducing an additional mass component to the envelope. In confirmation of the results of Myers et al. (1998), we find that this extra mass is lost on a shorter timescale than the protostellar accretion timescale. The bolometric temperature is calculated according to the optically thick case of Myers et al. (1998). We thus extend the opacity law approximation employed up to 60 to $120 \mu\text{m}$ with the same form and take the optically thick envelope throughout the early evolutionary stages. We have thus found here that an envelope mass

$$M_{\text{env}}(t) = M_{\text{inf}} \cdot (0.87 + \mu(t/t_o)^{-2\alpha}) \quad (11)$$

where $\mu = 2$ provides bolometric temperatures, timescales and masses consistent with the observed samples.

The envelope mass provides a testable prediction. This mass is not strongly dependent on the evolutionary path but is necessary to provide the optical depth out to a sufficiently large radius to permit the measured low bolometric temperature. The total mass is dominated by the outer regions of the envelope, while the total optical depth is controlled by the inner region (for all plausible density distributions such as $\rho \propto r^{-3/2}$, as assumed here). Hence, the mass is sensitive to the extent of the envelope. For this reason, we present three determinations of the envelope mass in Table 6. Masses derived from submillimetre observations yield quite low extended masses (André et al. (2000)), consistent with the absence of more mass than necessary to form the star and feed the jets (Smith (2000)). It is clear that both the observationally derived mass and model mass are sensitive to chosen physical parameters and both will need refining.

REFERENCES

André, P., Ward-Thompson, D., Barsony, M. 2000, in Protostars and Planets IV, 59
 Anglada, G., Rodríguez, L.F., 2002, Revista Mexicana de Astronomía y Astrofísica, 38, 12
 Barsony, M., Ward-Thompson, D., André, P., O'Linger, J., 1998, AJ, 509, 733
 Bontemps, S., André, P., Terebey, S., Cabrit, S., 1996, A&A, 311, 858
 Calvet, N., Hartmann, L.W., Strom, S.E., 2000, in Protostars & Planets IV, ed. V. Mannings et al., (Tucson, U. of Arizona Press), 377
 Chini, R., Ward-Thompson, D., Kirk, J.M., Nielbock, M., Reipurth, B., Sievers, A., 2001, A&A, 369, 155
 Clegg, P.E., Ade, P.A.R., Armand, C., et al., 1996, A&A, 315, L38
 Davis, C.J., Eislöffel, J., 1995, A&A, 300, 851
 Davis C.J., Smith M.D., Moriarty-Schieven G.H., 1998, MNRAS, 299, 825
 Davis, C.J., Ray, T.P., Eislöffel, J., Corcoran, D., 1997, A&A, 324, 263

Eislöffel, J., A&A, 2000, 354, 236

Eislöffel, J., Froebrich, D., 2004, in prep.

Eislöffel, J., Froebrich, D., Stanke, T., McCaughrean, M.J., 2003, ApJ, in press

Eislöffel, J., Smith, M.D., Davis, C.J., Ray, T.P., 1996, AJ, 112, 2086

Eislöffel, J., Ziener, R., Froebrich, D., 2004, in prep.

Froebrich, D., Eislöffel, J., 2004, in prep.

Froebrich, D., Scholz, A., 2003, A&A, in press

Froebrich, D., Smith, M.D., Eislöffel, J., 2002, A&A, 385, 239

Froebrich, D., Ziener, R., Eislöffel, J., AG Abstr. Ser., 18, 25

Gabriel, C., et al., 1997, in ASP Conf. Ser. Vol. 125, Astronomical Data Analysis Software and Systems (ADASS) VI, ed. G. Hunt & H.E. Payne, (San Francisco ASP), 108

Giannini, T., Nisini, B., Lorenzetti, D., 2001, ApJ, 555, 40

Gueth, F., Guilloteau, S., 1999, A&A, 343, 571

Gueth, F., Guilloteau, S., Dutrey, A., Bachiller, R., 1997, A&A, 323, 943

Hirose, S., Uchida, Y., Shibata, K., Matsumoto, R., 1997, PASJ, 49, 193

Kessler, M.F., Steinz, J.A., Anderegg, M.E., et al., 1996, A&A, 315, L27

Ladd, E.F., Hodapp, K.-W., 1997, ApJ, 475, 749

Laureijs, R.J., 1999, Point spread function fractions related to the ISOPHOT C100 and C200 arrays, ISO-Data centre, Astrophysics Division, ESA, Villafranca Spain, http://www.iso.vilspa.esa.es/users/expl_lib/PHT/c200fpsf02.ps.gz

Lefloch, B., Eislöffel, J., Lazareff, B., 1996, A&A, 313, L17

Lemke, D., Klaas, U., Abolins, J., et al., 1996, A&A, 315, L64

McCaughrean, M.J., Rayner, J.T., Zinnecker, H., 1994, ApJ, 436, L189

Moro-Martín, A., Noriega-Crespo, A., Molinari, S., Testi, L., Chernicharo, J., Sargent, A., 2001, A&A, 555, 146

Motte, F., André, P., 2001, A&A, 365, 440

Myers, P.C., Adams, F.C., Chen, H., Schaff, E., 1998, ApJ, 492, 703

Ouyed, R., Pudritz, R.E., 1997, ApJ, 482, 712

Rengel, M., Eislöffel, J., Hodapp, K.-W., 2003, in prep.

Rengel, M., Froebrich, D., Eislöffel, J., Hodapp, K., 2001, AG Abstr. Ser. 18, 66

Rengel, M., Froebrich, D., Hodapp, K., Eislöffel, J., 2002, In: The Origins of Stars and Planets: The VLT View, João Alves & Mark McCaughrean (ed.)

Saraceno P., André P., Ceccarelli C., Griffin M., Molinari S., 1996, A&A 309 827

Shu, F., Najita, J., Ostriker, E., Wilkin, F., Ruden, S., Lizano, S., 1994, ApJ, 429, 781

Smith M.D., 1998, Ap&SS, 261, 169

Smith, M.D., 2000, IraJ, 27, 25

Smith, M.D., 2002, In: The Origins of Stars and Planets: The VLT View, João Alves & Mark McCaughrean (ed.)

Smith, M.D., Brand, P.W.J.L., 1990, MNRAS, 245, 108

Smith, M.D., Froebrich, D., Eislöffel, J., 2003, ApJ, 592, 245

Stanke, T., 2000, Ph.D. thesis (AIP, Potsdam)

Strom, S.E., Strom, K.A., Carrasco, L., 1974, PASP, 86, 798

Tafalla, M., Myers, P.C., Mardones, D., Bachiller, R., 1999, A&A, 348, 479

Yu, K.C., Billawala, Y., Smith, M.D., Bally, J., Butner, H., 2000, AJ, 120, 1974

Zinnecker, H., McCaughrean, M.J., Rayner, J.T., 1998, Nature, 394, 862